First-principles treatment of vibrational broadening in x-ray excited valence band spectra for *n*-$SrTiO_3$(001)

Scott A. Chambers,[1] Deepnarayan Biswas,[2] Tien-Lin Lee,[2] Mark van Schilfgaarde,[3] and Peter V. Sushko[1]

[1]*Physical Sciences Division, Physical and Computational Sciences Directorate, Pacific Northwest National Laboratory, Richland, Washington 99352, USA*

[2]*Diamond Light Source, Ltd., Harwell Science and Innovation Campus, Didcot, Oxfordshire OX11 0DE, England, United Kingdom*

[3]*Materials Science Division, National Renewable Energy Laboratory, Golden, Colorado 80401, USA*

(Received 27 February 2024; revised 16 April 2024; accepted 18 April 2024; published 6 May 2024)

The valence band maximum (VBM) is an important quantity for semiconductors as it locates the Fermi level relative to the band edge. Accurate measurement of this quantity in near-surface regions of semiconductors by photoemission is a first step toward determining the electronic properties of heterostructures involving these materials. While extrapolating the leading edge of the valence band to the energy axis in photoemission spectra is a widely used way to find the VBM, this method can be ambiguous if the leading edge exhibits multiple slopes. Another way to determine the VBM is to fit the leading edge to an appropriately broadened, cross-section modulated theoretical density of states (DOS). Three kinds of broadening that should be included for maximum accuracy are those due to: (1) finite instrumental resolution, (2) valence hole lifetime, and (3) vibrational excitations. While steps (1) and (2) are straightforward to implement, (3) is more difficult because the appropriate amount of broadening is not known *a priori*. Here, we demonstrate that explicit inclusion of vibrational broadening using *ab initio* molecular dynamics facilitates accurate VBM determination for *n*-$SrTiO_3$(001). The total DOS is constructed by summing time-averaged projections at elevated temperature onto *s*-, *p*-, and *d* orbitals for the constituent atoms and modulating with the associated photoemission cross sections. Subsequent convolutions of the total DOS, first with a Gaussian of width equal to the experimental energy resolution and second with a Lorentzian to simulate valence hole lifetime effects, yield line shapes that reproduce the experimental leading edges rather well. The VBM is then given by the energy at which the vibrationally broadened total DOS (prior to the convolutions) goes to zero. The VBMs generated by this method quantitatively agree with those resulting from extrapolating from the middle of the measured leading edge for $SrTiO_3$.

DOI: 10.1103/PhysRevB.109.195115

I. INTRODUCTION

Experimental measurements of band-edge profiles across heterostructures consisting of semiconducting materials are essential for understanding the electronic properties of these systems [1–19]. Of ongoing interest is band alignment at interfaces, as well as band bending in individual films, at interfacial regions, and at surfaces. The latter can signal the depletion of carriers from, and dead-layer formation in, the near-surface region, which in turn can have deleterious effects on electronic transport [20,21]. X-ray photoelectron spectroscopy (XPS) has been widely used to measure band alignment and band bending in a variety of materials systems for decades. An early approach for accurately measuring band-energy profiles was conceived and utilized by Kraut *et al.* [1,3] and Waldrop *et al.* [2] in their studies of group IV and group III–V heterojunction band offsets and Schottky barriers, respectively. This method involves referencing shallow core levels (CLs) to the valence band maximum (VBM), all excited with soft x rays. So doing allows VB edges in different materials of a multilayer system to be tracked by measuring CL binding energies for elements found in those materials. CLs are far more intense and considerably easier to fit than VBs, leading to results that are more accurate than those that come directly from VB measurement and analysis. A key quantity needed to utilize this method is the energy difference between a specific CL and the VBM in a pure component material. Provided no chemical reactions occur at the interface during heterostructure formation, such energy differences can be used to track valence band offsets, built-in potentials, and Schottky barrier heights using heterostructure CL measurements. A high level of accuracy is essential in this endeavor to maximize its usefulness. A key step in the process is to carry out accurate, absolute binding-energy calibrations based on metal Fermi edges or shallow CLs, rather than using the C 1*s* peak from adventitious carbon [22]. The accuracy goal in these measurements should be a few hundredths of an electron volt (i.e., kT at 300 K) in order to maximize relevance to electronic transport at ambient temperature.

As described in detail in Kraut *et al.* [3], one way to obtain the VBM is to fit the VB leading edge to a theoretical density of states (DOS) modulated by the relevant photoemission transition probabilities (i.e., cross sections) and broadened by convolving with a Gaussian of width equal to the instrumental energy resolution. Another, much simpler method is to extrapolate the leading edge of the experimental VB spectrum

to the energy axis using linear least-squares fitting. However, since the leading edge is, in general, not linear throughout, an important question is which part of it should be used in the fitting procedure? Depending on the shape of the leading edge, significantly different VBM values, as determined by the intercepts, can be obtained depending on whether the data points are taken from the top, middle, or bottom section. Previous results indicate that at least for clean Si(001)-(2 × 1), the two methods yield the same VBM value to within experimental error, provided the linear regression is carried out in the middle portion of the leading edge so as to not incur error by including the instrumental-broadening induced tail at the bottom [23,24]. However, the DOS fitting approach was found to yield VBM values larger by ∼0.4 eV than those from the linear regression method for SrO, TiO_2 anatase, and $SrTiO_3$ epitaxial films deposited on Si(001) when the DOSs were calculated using density-functional theory (DFT) [23]. Much better agreement was found if self-consistent *GW* (sc-*GW*) theory was used to generate the DOS. (G = Green′s function and W = screened Coulomb interaction). In this case, the VBMs differ by only ∼0.1 eV for $SrTiO_3$ [24]. However, it has also been observed that neither the DOS fitting method nor the linear regression method works well for clean, single-crystal diamond samples, particularly when hard x rays are used [25].

The purpose of this study is to revisit the DOS fitting method and consider the role that vibrational broadening plays in determining the shape of the DOS. We base our investigation on $n-SrTiO_3(001)$, a prototypical complex oxide semiconductor of some interest. We employ state-of-the-art XPS and hard x-ray photoemission spectroscopy, along with sc-*GW* theory, DFT, and *ab initio* molecular dynamics (AIMD) simulations. $SrTiO_3$ (STO) is an insulator with an indirect (direct) band gap of 3.25 (3.75) eV [26]. STO can be converted to an *n*-type semiconductor either by doping the *A* site with a trivalent rare-earth metal, such as La or Dy, or the *B* site with a pentavalent transition metal, such as Nb [27,28]. It can also be made *n* type by the removal of oxygen from the lattice, thereby forming the oxygen vacancy (V_O) defect, which is a double donor in many oxides, including STO [17,18,29–32]. Valence band (VB) spectra excited using x rays effectively represent averages over the Brillouin zone and thus indicate the smaller of the two gap values, namely that corresponding to the indirect gap in STO, 3.25 eV, provided there is no band bending at the surface.

II. EXPERIMENTAL AND MODELING DETAILS

Unless otherwise noted, all measurements were carried out using bulk $SrNb_xTi_{1-x}O_3(001)$ ($x \leqslant 0.01$) single crystals. Laboratory-based XPS measurements were performed using unpolarized, monochromatic Al-Kα x rays (1486.7 eV) and Cr-Kα x rays (5405.5 eV). All synchrotron-based measurements were carried out on beamline I09 at Diamond Light Source using linearly polarized x rays ranging in energy from 460 to 6 keV. In all cases, VG/Scienta analyzers were used in angle-integrated mode to measure zone-averaged VB spectra. All samples were well grounded to the spectrometer, thereby facilitating the measurement of accurate absolute binding energies following calibration using metal (Au or Cu) Fermi edges.

The quasiparticle self-consistent *GW* approximation (QS*GW*) is a self-consistent form of Hedin's *GW* approximation [33]. Self-consistency eliminates the starting-point dependence, and as a result the discrepancies with experiment are much more systematic than in the case of conventional forms of *GW* [34–36]. The great majority of discrepancies with one- and two-particle properties in insulators originate from the omission of electron-hole interactions in the random-phase approximation (RPA) polarizability. By adding ladders to the RPA, electron-hole effects are taken into account. Generating W with ladder diagrams ($W \rightarrow \hat{W}$) has several consequences: most importantly, perhaps, screening is enhanced and W is reduced. This in turn reduces fundamental band gaps and also valence bandwidths. Agreement with experiment in both one-particle and two-particle properties is greatly improved. The theory and its application to a large number of both weakly and strongly correlated insulators is given in Ref. [37]. The importance of self-consistency in both QSGW and QSG$\hat{W}$ for different materials has been explored [36].

For the AIMD calculations, bulk $SrTiO_3$ was represented using the periodic model approach and the cubic supercell was constructed as a 4 × 4 × 4 extension of the crystallographic cell. The lattice parameters were fixed at the values corresponding to the ideal bulk STO (a_0 = 3.905 Å). The electronic structure calculations were performed using the Perdew-Burke-Ernzerhof for solids (PBEsol) exchange-correlation functional [38] as implemented in the VASP code [39,40]. A $+U$ correction for the Ti 3*d* states (U = 3 eV) was applied according to the scheme proposed by Dudarev *et al.* [41]. This correction was applied to prevent crossover in the character of the electronic states of the valence- and conduction bands that may occur due to fluctuations in the band edges, which invariably occur as the supercell is heated. Such crossover would result in artificially inverting the electron population and, therefore, require a large number of self-consistent field (SCF) iterations to recover. We thus used a $+U$ value large enough to maintain sufficient separation between the VBM and CBM, but not so large as to influence the structural evolution. In an earlier study [42], we found that U = 4 eV provides reasonable agreement between model defects in STO and their experimental signatures. In this study, we found that the SCF procedure converges relatively quickly even with a smaller magnitude of the correction.

The core electrons were represented using the projector augmented wave (PAW) pseudopotentials [43]. The plane-wave basis-set cutoff was set at 400 eV, and calculations were carried out in non–spin-polarized mode at the Γ point only. As a test of the adequacy of the Γ-point sampling, we show in Fig. 1 valence band DOSs obtained by averaging over the DOSs of five instantaneous configurations generated in our AIMD simulations at 1000 K. The five configurations were separated by 2 ps of simulation time. The DOS calculated using 1 × 1 × 1 (Γ point only), 2 × 2 × 2, and 3 × 3 × 3 *k* grids were convoluted with Gaussian-type functions of full width at half maximum (FWHM)= 0.1 eV [Fig. 1(a)] and then further broadened to account for instrumental and valence hole lifetime effects [Fig. 1(b)]. While the choice of *k* grid makes some very slight differences at certain points within the raw DOS [Fig. 1(a)], the leading edge is not affected in

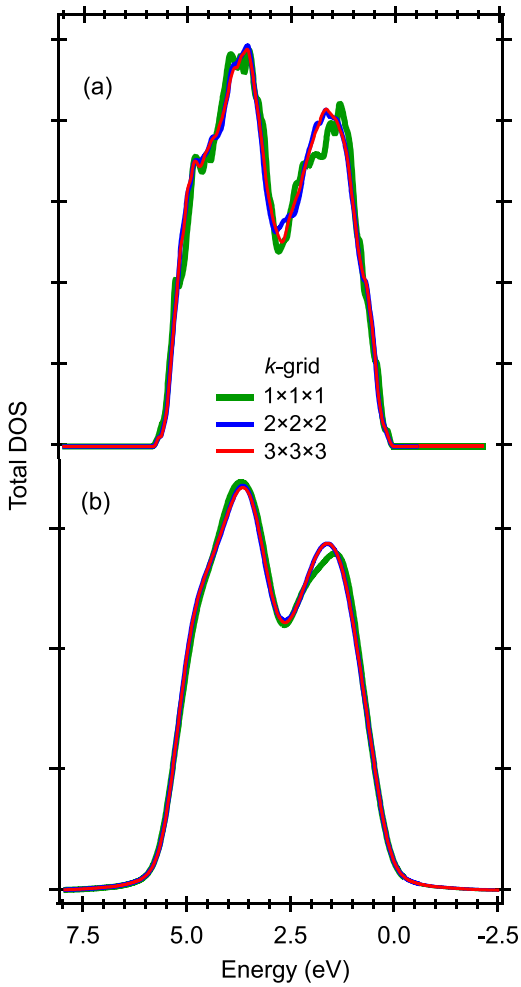

FIG. 1. Test of the dependence of the total DOS calculated using density-functional theory PBEsol on the choice of k-grid density for $SrTiO_3$. (a) Average over five AIMD configurations ($T = 1000$ K) broadened with Gaussians of FWHM of 0.1 eV. (b) The calculated DOSs broadened to account for the experimental resolution and valence hole lifetime. See text for details.

any significant way, particularly at the intersection with the energy axis, which is critical for determining the VBM. Which minor differences are present in the thermally broadened DOS [Fig. 1(a)] are gone after instrumental and lifetime broadening [Fig. 1(b)]. In addition, we note that the density of the k grid has little effect on the dynamics of the system as well. In particular, after accounting for the energy offset, the total energies calculated for the five selected configurations differ by less than 0.2 meV per atom. Similarly, the projection of normalized forces acting on individual atoms calculated using the $2 \times 2 \times 2$ and $3 \times 3 \times 3$ k grids onto the similarly normalized forces calculated using the $1 \times 1 \times 1$ grid differs from unity by less than 10^{-5}. Therefore, we concluded that limiting our DOS simulations to the Γ point is fully adequate. The energy convergence criterion was set to 10^{-5} eV. The microcanonical ensemble (*NVE*) was adopted for *ab initio* AIMD simulations. The simulation time step was 1 fs. The AIMD structural configurations, one-electron band energies, and densities of states projected on the s-, p-, and d shells of each atom were recorded every 200 time steps for further analysis. The simulations were conducted for average AIMD temperatures of ∼500, 1000, and 1500 K.

III. RESULTS

To motivate this investigation, we present in Fig. 2 analyses of the VB spectra for $SrNb_{0.01}Ti_{0.99}O_3(001)$ excited with laboratory-source Al-Kα x rays [Fig. 2(a)] and with synchrotron-generated x rays of energies 3 keV [Fig. 2(b)] and 6 keV [Fig. 2(c)]. We have overlaid each spectrum with a sum of projected DOS (p-DOS) generated using QSGW theory at $T = 0$ K, with each p-DOS modulated by the relevant atomic photoemission cross section [44,45] prior to making the sum. The raw DOS is thus given by

$$N(E_b, \hbar\omega) = \sum_{i,j} \sigma_{i,j}(\hbar\omega) N_{i,j}(E_b). \tag{1}$$

Here, E_b is the binding energy, the sums are over both atoms (i) and orbitals (j), and $N_{i,j}$ are the p-DOS for O $2s$, O $2p$, Sr $5s$, Sr $4p$, Sr $4d$, Ti $4s$, Ti $4p$, and Ti $3d$ orbitals. The atomic cross sections are given by $\sigma_{i,j}$. Also shown in each panel is the same raw DOS broadened with a Gaussian of full width at half maximum equal to the total experimental energy resolution (x rays plus analyzer), and with a Lorentzian of FWHM equal to 0.20 eV [46] to account for valence hole lifetime. The Lorentzian convolution step was not taken in the original DOS fitting model [3], but is important for maximum realism in the simulation. A linear least-squares fit of the middle section of the experimental VB leading edges and its extrapolation to the energy axis is shown as an inset in each panel, along with the resulting VBM. There is a clear difference between the extrapolation-based VBM values taken from the spectrum excited with Al-Kα x rays [Fig. 2(a)] and those generated by synchrotron light [Figs. 2(b) and 2(c)], and this difference is discussed below.

Based on the value of the indirect gap and position of the conduction band minimum (CBM) relative to the Fermi level expected from a graphical solution of the charge-neutrality equation for the doping density used here [47], we note that to within experimental error, extrapolation of the leading edge in the middle section of the Al-Kα measurement yields the VBM value expected for flatband, degenerately doped n-STO(001), 3.25 eV. However, despite the accuracy of QSGW theory, agreement between theory and experiment is not particularly good for any of the measured spectra, especially along the leading edges which are critical for VBM determination. While the experimental leading edges are linear over at least the middle section in all cases, the broadened theoretical DOS (red curves) are not linear anywhere along the leading edge. Therefore, quantitative nonlinear least-squares fitting of the experimental leading edges to the broadened DOSs and subsequent extraction of the VBMs from the energy at which the raw DOSs go to zero is not useful. Nevertheless, we can align the entire experimental VB and the broadened DOS (red) by eye and apply the resulting shifts to the raw DOSs (green) to see where the latter go to zero. The corresponding VBM values are also shown in Fig. 1. We note that the estimated VBMs from this method agree reasonably well with those

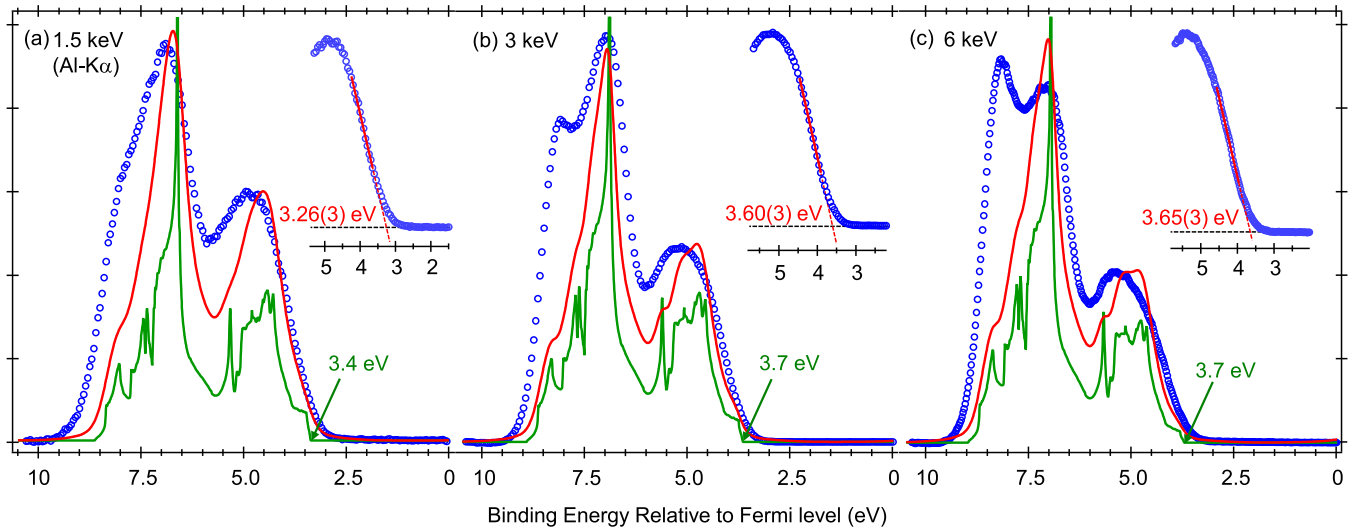

FIG. 2. Experimental valence band spectra for $SrNb_{0.01}Ti_{0.99}O_3(001)$ excited at different x-ray energies (blue) and compared to theoretical DOS for STO as calculated using quasiparticle self-consistent *GW* theory (green). The individual projected DOS were first multiplied by the relevant photoemission cross sections and then summed [Eq. (1)]. The summed DOS were then broadened with a Gaussian to account for instrumental resolution and a Lorentzian to capture the influence of the valence hole lifetime (red). The Gaussian FWHMs are 0.45, 0.40, and 0.25 eV for x-ray energies of 1.5 (a), 3 (b), and 6 (c) keV, respectively. The Lorentzian width was taken to be 0.20 eV in all cases. In each case, alignment of experiment and the broadened DOS is done by eye and an estimate of the VBM is taken from the energy at which the raw DOS goes to zero. Shown as insets are expanded views of the leading edges of the VB spectra along with linear least-square fits and extrapolations to the energy axis to yield values for the VBM. The uncertainty in the three VBM values is ±0.03 eV.

from linear regression analysis of the experimental leading edges, as shown in the insets. However, the agreement is fortuitous because the alignments of the broadened DOSs and the experimental spectra are subjective and not supported by quantitative fitting. Hence, we seek a more satisfactory way to fit theory and experiment.

One solution to this problem is overbroadening the raw DOS using a Gaussian width significantly greater than the experimental resolution, as illustrated in Fig. 3 for the spectrum in Fig. 2(a). Here, we broaden with a Gaussian of width equal to twice the instrumental broadening, 0.90 eV, instead of 0.45 eV as is used in Fig. 2(a). While agreement along the leading edge is considerably better than that seen in Fig. 2(a), the energy at which the raw DOS goes to zero is still higher than the expected value by 0.13 eV, i.e., a factor of 4 too large to be accounted for based the uncertainty (±0.03 eV). Additionally, arbitrarily overbroadening lacks rigor because the extent of broadening becomes an adjustable parameter that can maximize the similarity between the broadened DOS and the measured spectrum along the leading edge, while not yielding a VBM value sufficiently close to the correct value. Likewise, if spectra are measured with poorer energy resolution, it is in general easier to obtain good fits to broadened theoretical DOSs because substantive differences between theory and experiment are effectively hidden [23,48]. As we demonstrate below, *the most accurate results are forthcoming when all extrinsic sources of broadening are accurately taken into account in calculating the DOS.* In what follows, we show that the missing factor is thermal broadening at the experimental temperature of ∼300 K which is missing from theory, since the DOSs were calculated at $T = 0$ K. We demonstrate that the DOSs generated for STO at temperatures well above 0 K and averaged over time using structures generated by

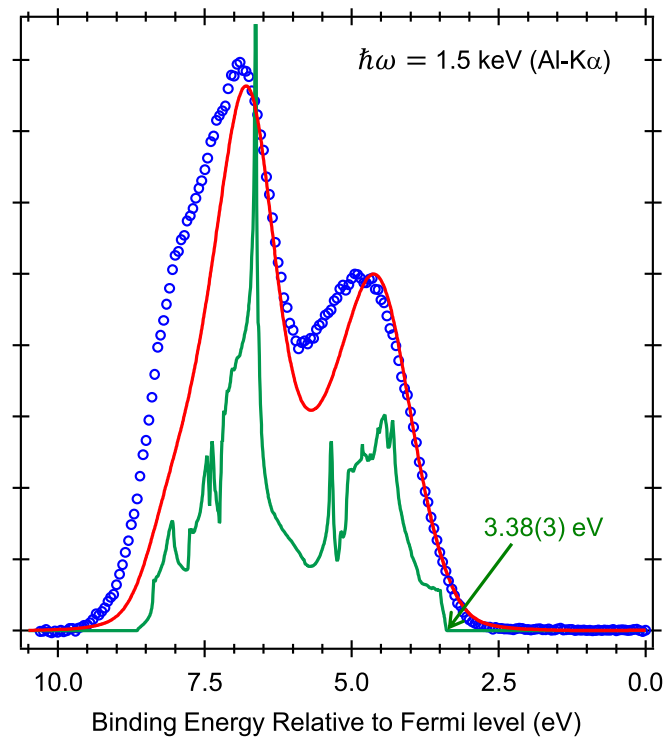

FIG. 3. The STO VB spectrum [as shown in Fig. 2(a)] overlapped with the cross-section modulated DOS calculated using QS*GW* theory that was broadened with a Gaussian of FWHM = 0.90 eV followed by a Lorentzian of FWHM = 0.20 eV. The 0.90-eV FWHM is twice the value of the actual experimental resolution. This figure illustrates that artificially overbroadening can result in superior agreement with theory, but still yields the wrong value for the VBM.

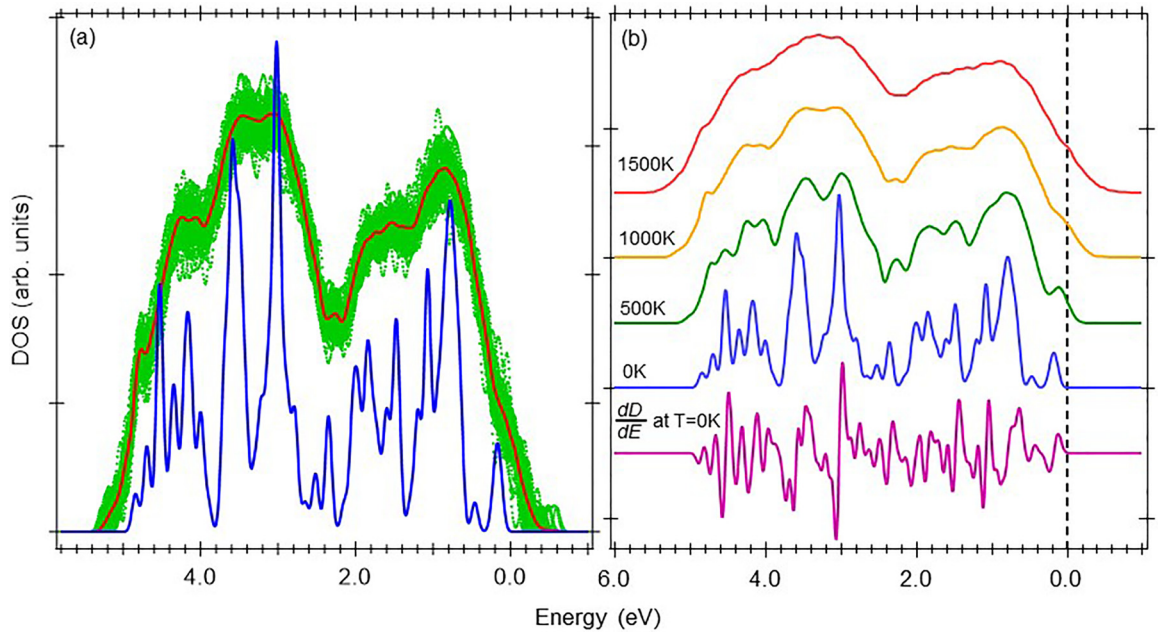

FIG. 4. (a) Fifty individual contributors to the density of states calculated by *ab initio* molecular dynamics at a simulation temperature of 1000 K (green). The DOSs were calculated every 200 fs for a total sampling time of 10 ps. The energy grid spacing was 0.0082 eV. Shown in red is the average of the 50 individual DOS sets, while the DOS for the static lattice with the equilibrium structure at $T = 0$ K is shown in blue. (b) Time-averaged DOSs as described for panel (a) at different simulation temperatures show the broadening effect of progressively higher temperature. The DOS and its first derivative go to zero at precisely the same energy for $T = 0$ K.

AIMD lead to simulated spectra in excellent agreement with experiment.

Figure 4(a) shows the time evolution of the STO VB total DOS calculated using the DFT in green. QS*GW* theory was not used because the number of individual electronic structure calculations that must be performed to carry out an accurate AIMD simulation is prohibitively high. The DFT DOSs were averaged over 50 configurations obtained by AIMD simulations (using the *NVE* ensemble) with an average temperature of 1000 K. The time interval between the AIMD configurations selected for the DOS calculations was set to 200 fs. The calculated DOS thus corresponds to sampling over a total time of 10 ps. The one-electron band energies corresponding to thermally excited configurations at the end of each 200-fs time interval were collected. The time-averaged DOS [shown in red in Fig. 4(a)] was generated by smearing the one-electron band energies using Gaussians of FWHM equal to 0.1 eV. The DOS for the static lattice at $T = 0$ K, also broadened using Gaussians of width 0.1 eV, is shown in blue. Since the simulation time and the supercell size are orders of magnitude smaller than the duration of the experiment and the physical dimensions of the crystal, respectively, we mimicked faster averaging over the thermally deformed configurations by performing the MD simulations at elevated temperatures (up to 1500 K). The broadening effect of the MD simulation temperature on the time-averaged total DOS is shown in Fig. 4(b). The DOSs at elevated temperature resemble experiment much more closely than does the one calculated at $T = 0$ K.

Seeing that AIMD simulations of vibrational effects broaden the total DOS in ways that cause them to look more like experiment, we now explore their effect on projected (p-)DOS. To do so, we project the total DOS onto the *s*-, *p*-, and *d* orbitals of all Sr, Ti, and O atoms for the same 50 AIMD configurations. Here, we use a simulation temperature of 1000 K. We then calculate time averages for each p-DOS and sum after multiplying each by the appropriate cross section. We then convolve with a Gaussian of width equal to the experimental resolution and a Lorentzian of width equal to 0.20 eV to account for hole lifetime broadening, as described above.

The rationale for using AIMD simulations carried out at $T = 1000$ K rather than 300 K has to do with the "size-time" gap between simulation and experiment. We note that since the dimensions of the simulated crystal are orders of magnitude smaller than the actual sample, and the simulation time is orders of magnitude smaller than the true measurement time, the space of thermally disordered configurations calculated at 300 K is undersampled. We thus use AIMD simulations at elevated temperature to accelerate the sampling of these thermally disordered configurations. From our analysis of simulations performed at 300, 500, 1000, and 1500 K, the DOS obtained at 1000 K shows the best agreement with the experimental data after accounting for instrumental and lifetime broadening. Therefore, we chose this DOS as the best representation of the true VB spectrum.

We show in Fig. 5 the experimental spectra seen in Fig. 2 overlaid with the best-fit DOSs resulting from the MD simulations. The raw, vibrationally broadened DOSs shown in green in each panel, and the same after convolutions for instrumental and lifetime effects shown in red, have been shifted to the energy that yields the best fit of the fully broadened DOSs (red) to experiment (blue). Hereafter, we refer to these fully broadened DOSs as our model spectra. To do the fit, the model spectra were scaled to the experimental intensities in the leading-edge regions and least-squares fits

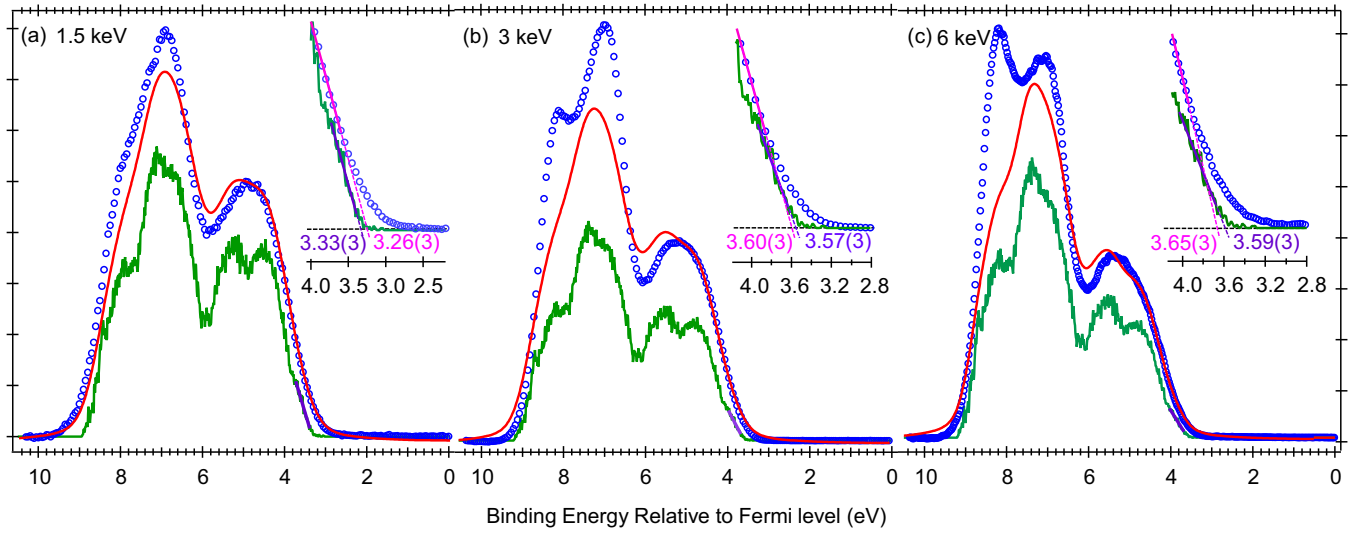

FIG. 5. Fitting the VB spectra measured at different x-ray energies using raw DOS constructed by summing projected DOS averaged over time at an MD simulation temperature of 1000 K. (See Fig. 6 for the dependences of the quality of the fit on the VBM value for each spectrum.) In all cases, the individual p-DOS were multiplied by the appropriate photoemission cross sections (green) and the sums of p-DOS were broadened by convolution with a Gaussian for instrumental effects and a Lorentzian for valence hole lifetime (red). The same Gaussian and Lorentzian widths were used as in Fig. 1. The p-DOS were calculated using DFT generalized gradient approximation (GGA) PBEsol + U with the U value of 3 eV for Ti 3d states. The insets show extrapolations of linear regression lines from fits at the bottom of the raw DOS (prior to convolutions) and from the middle of the experimental spectra, along with the associated VBM values. The excellent agreement establishes that linear regression based on points in the middle of the experimental leading edge yields a quantitatively accurate VBM. The uncertainty in the VBM values is ±0.03 eV.

were performed using a single fitting parameter, the binding energy. The dependence of the goodness of the fit is shown for each dataset in Fig. 6. The vibrationally broadened DOSs (green in Fig. 5) were then shifted by the same energies as the best-fit model spectra in each panel. Since we did not apply Gaussian broadening (FWHM = 0.1 eV) to the individual p-DOS, the summed, cross-section modulated p-DOSs (green) show more scatter than what is seen in the total DOSs [Fig. 4(b)]. One consequence of this fact is that the raw DOSs in Fig. 5 do not go cleanly to zero at unique energies on the low binding-energy sides, as do those in Fig. 4(b); there is some residual DOS within the first ∼0.2 eV to lower binding energy from what would otherwise appear to be the true VBM. To address this reality, we performed linear least-squares fits on the bottom sections of the vibrationally broadened DOS leading edges to determine the VBMs, as seen in purple in each of the three panels of Fig. 5. Expanded views of the portions of the summed, cross-section modulated p-DOSs and

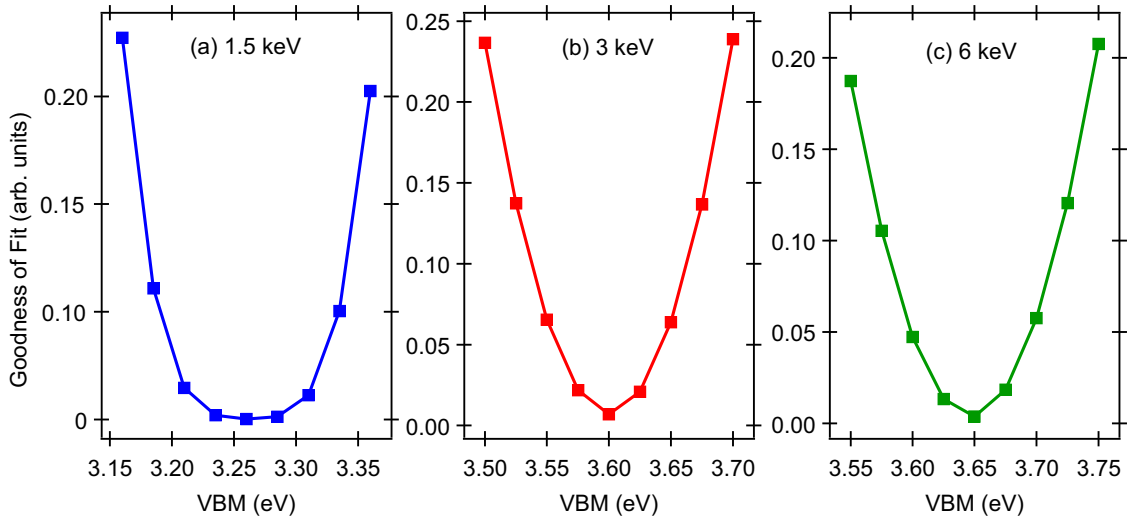

FIG. 6. Least-squares determination of the VBM from fitting the experimental lead edges shown in Fig. 4 to fully broadened DOSs and finding the binding energy at which the corresponding vibrationally broadened DOSs go to zero.

the experimental spectra close to the VBMs, along with their respective linear regression lines, are shown as insets, along with the resulting VBM values. The agreement between the model and experimental spectra is excellent at all three x-ray energies. The pairs of VBMs in the insets agree to within a few hundredths of an electron volt in all three cases. Significantly, this result shows that fitting the leading edge to a theoretical DOS that has been properly broadened for thermal effects, instrumental resolution, and valence hole lifetime allows one to assess the accuracy of linear regression and extrapolation to the energy axis by providing an objective, rigorously determined standard. In the case of STO, choosing points in the middle of the leading edge for linear regression analysis leads to the best results. However, in using this method of analysis for other complex materials, each system should be analyzed as described above because the detailed shape of the leading edge is material dependent.

Finally, we address the curious result that the VBM values obtained using linear regression of the middle part of the leading edge with x rays from the synchrotron (see Figs. 2 and 5) are ∼0.4 eV larger than that measured using Al-Kα x rays. Indeed, we have measured 13 sets of CL and VB spectra taken from different samples at different synchrotron x-ray energies ranging from 1.5 to 6 keV and have consistently measured VBM values ranging from 3.4 to 3.9 eV. In contrast, measurements taken using laboratory-source Al-Kα x rays fall in the range of 3.1–3.3 eV, depending on the extent of the band bending [49,50]. Moreover, one measurement employing laboratory-source Cr-Kα x rays (5.4 keV) yielded a value of 3.3 eV. Interestingly, the CL and VB spectra track approximately, but not perfectly, with each other across the datasets, as seen in the top and middle panels of Fig. 7. As a result, the energy differences between these core levels and the VBM vary less than the VBM itself, as seen by comparing middle and bottom panels in Fig. 7.

We consider four possible causes for this unusual result: (1) inaccurate energy calibrations, (2) nuclear recoil, (3) static charging, and (4) V_O creation by the incident beam, leading to downward band bending in the near-surface region. On binding-energy calibration, we note that each of these measurements was accompanied by a metal Fermi-edge measurement that was fit to a family of broadened Fermi functions, resulting in an absolute energy calibration accurate to ±0.02 eV, and a definitive value for the extent of instrumental broadening. Therefore, inaccurate energy calibration is not the cause. Regarding nuclear recoil, inspection of Fig. 7 does not show a monotonic dependence of binding energy on x-ray energy, as expected for nuclear recoil. Static charging results from the buildup of positive charge where x-ray exposure has occurred and photoelectrons have been emitted. If there is inadequate electron flow back from the grounded plate to which the sample is mounted, anomalously high binding energies will result. The likelihood of static charging increases with x-ray brilliance. Indeed, despite the relatively high doping level in our Nb:STO crystals, significant charging was observed when using a fully focused beam and optimized undulator settings. We thus defocused the beam in plane and detuned the undulator until the CL binding energies dropped and converged to constant values. However, it is possible that a slight imbalance between the photocurrent and the compensating

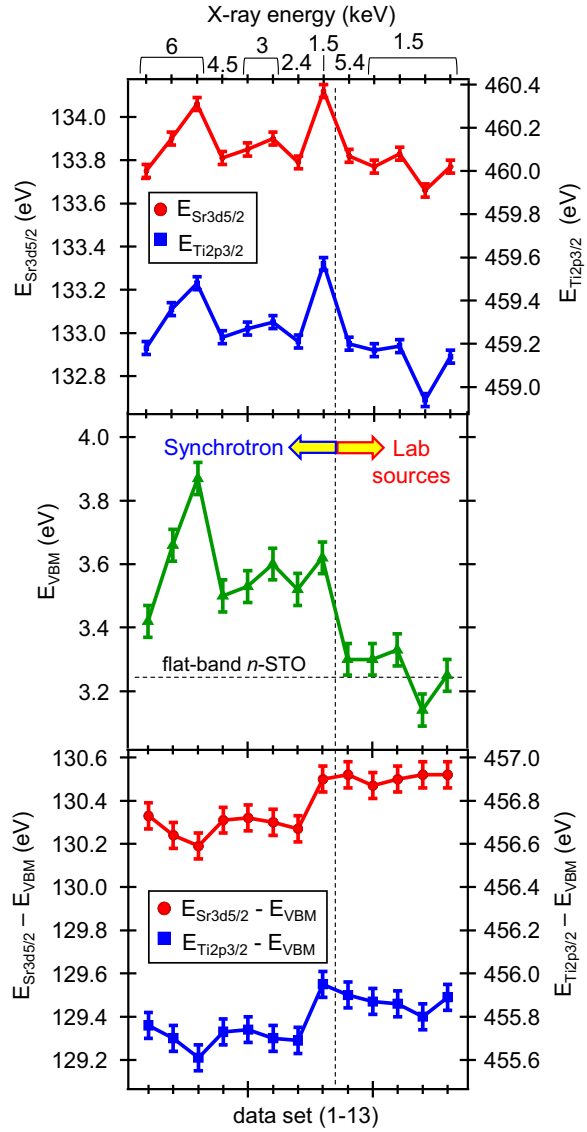

FIG. 7. Core-level binding energies, VBM values, and CL-VBM energy differences for 14 different $SrNb_xTi_{1-x}O_3(001)$ crystals with $x \leqslant 0.01$ taken with a range of x-ray energies, generated by both laboratory-based sources and synchrotron light. The two core levels and the VBM track in ways that are qualitatively the same across the datasets. However, the variations in the CL binding energies are smaller, resulting in more modest changes in CL-VBM values compared to the VBM itself.

current was still occurring, resulting in small shifts to higher binding energy. That said, V_O creation leading to downward band bending may also be occurring, despite our efforts to minimize the incident beam brilliance.

One way to discriminate between static charging and downward band bending due to V_O creation is to find the Fermi level *within* the sample itself. This can be done by tuning the x rays to an energy near the Ti $L_3 \rightarrow M_{4,5}$ x-ray absorption resonance and thus utilize the resulting enhancement of photoemission from the Ti-3d-derived states at the bottom of the CB, which are partially occupied due to n-type doping. Resonant enhancement occurs because the coherent two-step process $2p^6 3d^n + \hbar\omega_{res} \rightarrow 2p^5 3d^{n+1} \rightarrow$

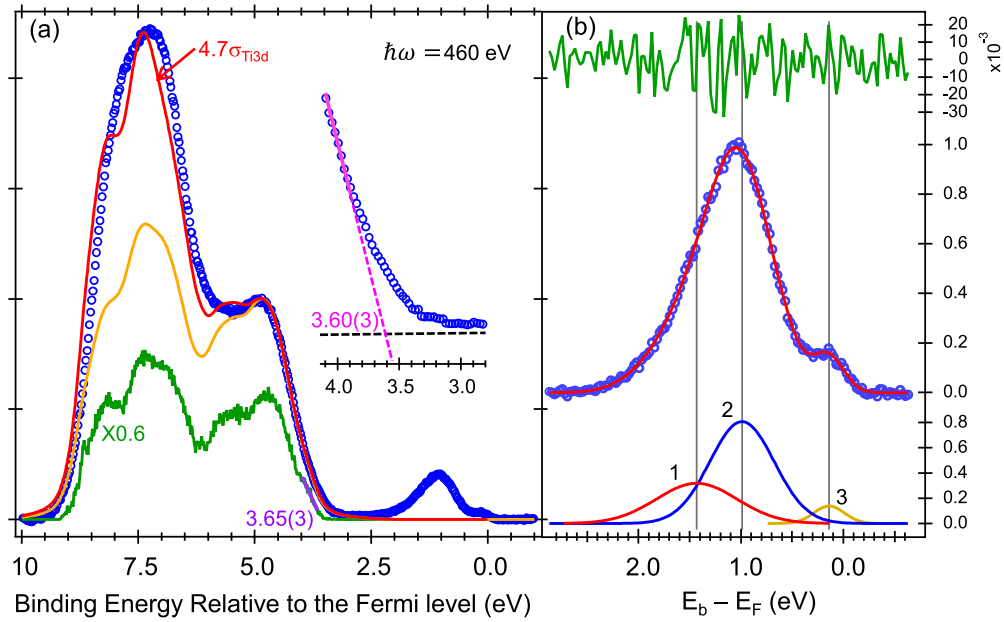

FIG. 8. VB spectrum for a homoepitaxial film of Dy-doped STO(001) taken at an x-ray energy of 460 eV. The VB proper was fit to an AIMD DOS, as described in conjunction with Fig. 3. The instrumental resolution in this measurement was 0.15 eV. The x-ray energy was judiciously chosen to be close to the Ti $L_3 \rightarrow M_{4,5}$ x-ray absorption resonance, thus resulting in considerable photoemission intensity enhancement from Ti-3d-derived states at the bottom of the CB. This approach provides a way to distinguish between static charging and downward band bending as candidate causes for the anomalously high VBM generated with synchrotron light, as described in the text.

$2p^6 3d^{n-1} + e^-$ yields the same final state as the direct photoemission channel $2p^6 3d^n + \hbar\omega \rightarrow 2p^6 3d^{n-1} + e^-$excited away from resonance, but with much more intensity. The intensity of this CB state is too low to detect by direct photoemission if the dopant concentration is ∼1 at. % or less, as in the present case [42,50]. In contrast, resonant enhancement is expected to be substantial and give rise to a readily detectable quasiparticle (QP) feature near the Fermi level. If this feature appears at the expected binding energy and the VBM is larger than expected, then downward band bending is indicated. If instead the QP peak shifts to higher binding energy from its expected value by an amount equal to the VBM shift from its expected value, then static charging is the more likely explanation.

We show in Fig. 8(a) the VB spectrum excited using 460 eV x rays for a 146-nm $Dy_{0.001}Sr_{0.999}TiO_3$(001) film grown by hybrid molecular-beam epitaxy (MBE) on an undoped STO(001) substate with an 8-nm STO buffer layer. The VB feature at ∼7.5 eV is much more intense than those found at other x-ray energies (see Fig. 5) and is also more intense than the model spectrum, as calculated using the AIMD method described above (gold). This result is to be expected because this VB feature has considerable Ti 3d character and is thus enhanced at $\hbar\omega = 460$ eV due to strong Ti $L_3 \rightarrow M_{4,5}$ x-ray absorption. Indeed, if the Ti 3d atomic cross section is increased by a factor of 4.7 and the model spectrum is recalculated (red), the intensity of the feature at 7.5 eV is in much better agreement with experiment. Both the model spectrum with the standard atomic cross section (gold) and that in which the Ti 3d cross section has been increased by a factor of 4.7 (red) fit the experimental leading edge equally well and result in the same VBM within experimental error, 3.60(3) eV, as those measured for $\hbar\omega = 3$ and 6 keV (see Fig. 5). However, we also see other features in the gap and near the Fermi level [Fig. 7(b)] that result from resonant enhancement of Ti-3d-derived states [51–57]. The Fermi level falls at the inflection point of the leading edge in the QP feature (peak 3), as expected if there is no charging. Therefore, charging can be eliminated and downward band bending due to V_O creation is the more credible explanation. In support of this conclusion, we note that the acquisition time for the spectrum obtained using Al-Kα x rays [Fig. 5(a)] is a factor of 4 longer than that for 3-keV synchrotron light [Fig. 4(b)]. When one considers the superior counting statistics in Fig. 5(b) compared to Fig. 5(a), the effective x-ray exposure time, which can be thought of as the time required to obtain the VB spectrum with a certain number of total counts, is more than 4 times longer in Fig. 5(a) than in Fig. 5(b). Thus, it is not surprising that the much more brilliant synchrotron beam would generate some oxygen vacancies, resulting in downward band bending, whereas the laboratory Al-Kα source would not.

Returning to Fig. 7, we expect the energy shifts from sample to sample to be nearly the same for all CLs and the VB, resulting in the very similar (within ±0.05 eV) energy differences among the various features. However, as seen in Fig. 7, the maximum variations in ($E_{Ti2p3/2}$–E_{VBM}) and ($E_{Sr3d5/2}$–E_{VBM}) are 0.34 and 0.33 eV, respectively, whereas ($E_{Ti2p3/2}$–$E_{Sr3d5/2}$) spans a range of only 0.18 eV across the dataset. This result may reflect the dynamic nature of V_O creation by the incident beam and annihilation via O diffusion from the bulk. This phenomenon could in turn lead to time-dependent shifts in the binding energies of different features measured over the course of the experiment.

IV. SUMMARY

We demonstrate that a first-principles treatment of vibrational broadening by *ab initio* molecular dynamics leads to a rigorously defensible determination of the VBM for $n-SrTiO_3$. Using this result as a standard, we show that extrapolation of the linear portion of the experimental leading edge measured by photoemission and taken from the middle region yields a VBM value that is accurate to within a few hundredths of an electron volt. These results are important because the VBM is a fundamental quantity that allows x-ray-generated core-level electron spectra to be used to track band-edge profiles in heterostructures of complex materials. We also show that n-$SrTiO_3$ spectra generated using synchrotron light can yield binding energies that are slightly higher than expected for this material in the flatband state because oxygen vacancy creation and downward band bending can occur, even when the brilliance of the incident beam is significantly reduced.

ACKNOWLEDGMENTS

This work was supported by the U.S. Department of Energy (DOE), Office of Science, Basic Energy Sciences, Materials Sciences and Engineering Division, Synthesis and Processing Science program (Grant No. PNNL FWP 10122). This research used resources of the National Energy Research Scientific Computing Center, a DOE Office of Science User Facility supported by the Office of Science of the U.S. Department of Energy under Contract No. DE AC02-05CH11231 using NERSC Award No. BES-ERCAP0028636. M.v.S was supported by the Computational Chemical Sciences program within the Office of Basic Energy Sciences, U.S. Department of Energy under Contract No. DE-AC36-08GO28308. The authors are grateful to Prof. Bharat Jalan (University of Minnesota) and Prof. Alex Gray (Temple University) for the MBE-grown Dy-doped STO homoepitaxial film sample and the CrKα measurement, respectively.

[1] E. A. Kraut, R. W. Grant, J. R. Waldrop, and S. P. Kowalczyk, Precise determination of the valence-band edge in x-ray photoemission spectra – application to measurement of semiconductor interface potentials, Phys. Rev. Lett. **44**, 1620 (1980).

[2] J. R. Waldrop, Interface chemistry and electrical-properties of tungsten Schottky-barrier contacts to GaAs, Appl. Phys. Lett. **41**, 350 (1982).

[3] E. A. Kraut, R. W. Grant, J. R. Waldrop, and S. P. Kowalczyk, Semiconductor core-level to valence-band maximum binding-energy differences – precise determination by x-ray photoelectron-spectroscopy, Phys. Rev. B **28**, 1965 (1983).

[4] R. W. Grant and J. R. Waldrop, Variation of n-GaAs (100) interface Fermi level by Ge and Si overlayers, J. Vac. Sci. Technol. B **5**, 1015 (1987).

[5] S. A. Chambers, V. A. Loebs, and D. H. Doyle, The role of ultrathin AlAs interlayers in determining the interface Fermi energy of the epitaxial NiAl /AlAs/n-GaAs(001) system, J. Vac. Sci. Technol. B **8**, 985 (1990).

[6] M. H. Hecht, Photovoltaic effects in photoemission-studies of Schottky-barrier formation, J. Vac. Sci. Technol. B **8**, 1018 (1990).

[7] J. P. Landesman, G. Jezequel, J. Olivier, M. Larive, J. Thomas, A. Talebibrahimi, and J. E. Bonnet, Reactivity, growth mode, and kinetics of the Fermi level pinning at the Ni/GaAs(110) interface, J. Vac. Sci. Technol. B **9**, 2122 (1991).

[8] S. A. Chambers and T. T. Tran, Geometric structure at the Si/GaAs(001) interface - the relationship to AlAs/Si/GaAs band offsets, Phys. Rev. B **47**, 13023 (1993).

[9] A. Franciosi, L. Sorba, G. Bratina, and G. Biasiol, Modification of heterojunction band offsets at III-V/IV/III-V interfaces, J. Vac. Sci. Technol. B **11**, 1628 (1993).

[10] A. Franciosi and C. G. Van de Walle, Heterojunction band offset engineering, Surf. Sci. Rep. **25**, 1 (1996).

[11] R. Ludeke, The metal-semiconductor interface, Handb. Surf. Sci. **2**, 749 (2000).

[12] C. Capan, G. Y. Sun, M. E. Bowden, and S. A. Chambers, Epitaxial Cr on $n-SrTiO_3(001)$ - an ideal Ohmic contact, Appl. Phys. Lett. **100**, 052106 (2012).

[13] A. Klein, Energy band alignment at interfaces of semiconducting oxides: A review of experimental determination using photoelectron spectroscopy and comparison with theoretical predictions by the electron affinity rule, charge neutrality levels, and the common anion rule, Thin Solid Films **520**, 3721 (2012).

[14] S. A. Chambers, M. Gu, P. V. Sushko, H. Yang, C. M. Wang, and N. D. Browning, Ultralow contact resistance at an epitaxial metal/oxide heterojunction through interstitial site doping, Adv. Mater. **25**, 4001 (2013).

[15] R. T. Tung, The physics and chemistry of the Schottky barrier height, Appl. Phys. Rev. **1**, 011304 (2014).

[16] S. A. Chambers and P. V. Sushko, Probing energy landscapes in multilayer heterostructures: Challenges and opportunities, APL Mater. **7**, 110904 (2019).

[17] Z. H. Lim, N. F. Quackenbush, A. N. Penn, M. Chrysler, M. Bowden, Z. Zhu, J. M. Ablett, T.-L. Lee, J. M. LeBeau, J. C. Woicik, P. V. Sushko, S. A. Chambers, and J. H. Ngai, Charge transfer and built-in electric fields between a crystalline oxide and silicon, Phys. Rev. Lett. **123**, 026805 (2019).

[18] M. Chrysler, J. Gabel, T. L. Lee, A. N. Penn, B. E. Matthews, D. M. Kepaptsoglou, Q. M. Ramasse, J. R. Paudel, R. K. Sah, J. D. Grassi, Z. Zhu, A. X. Gray, J. M. LeBeau, S. R. Spurgeon, S. A. Chambers, P. V. Sushko, and J. H. Ngai, Tuning band alignment at a semiconductor-crystalline oxide heterojunction via electrostatic modulation of the interfacial dipole, Phys. Rev. Mater. **5**, 104603 (2021).

[19] R. T. Tung and L. Kronik, Quantitative explanation of the Schottky barrier height, Phys. Rev. B **103**, 035304 (2021).

[20] A. Ohtomo and H. Y. Hwang, Surface depletion in doped $SrTiO_3$ thin films, Appl. Phys. Lett. **84**, 1716 (2004).

[21] S. A. Chambers, D. Lee, Z. Yang, Y. Huang, W. Samarakoon, H. Zhou, P. V. Sushko, T. K. Truttmann, L. W. Wangoh, T.-L. Lee, J. Gabel, and B. Jalan, Probing electronic dead layers in homoepitaxial n-$SrTiO_3(001)$ films, APL Mater. **10**, 070903 (2022).

[22] G. Greczynski and L. Hultman, X-ray photoelectron spectroscopy: Towards reliable binding energy referencing, Prog. Mater Sci. **107**, 100591 (2020).

[23] S. A. Chambers, T. Droubay, T. C. Kaspar, and M. Gutowski, Experimental determination of valence band maxima for $SrTiO_3$, TiO_2, and SrO and the associated valence band offsets with Si(001), J. Vac. Sci. Technol. B **22**, 2205 (2004).

[24] S. A. Chambers, T. Droubay, T. C. Kaspar, M. Gutowski, and M. van Schilfgaarde, Accurate valence band maximum determination for $SrTiO_3$(001), Surf. Sci. **554**, 81 (2004).

[25] J. Lischner, S. Nemsák, G. Conti, A. Gloskovskii, G. K. Pálsson, C. M. Schneider, W. Drube, S. G. Louie, and C. Fadley, Accurate determination of the valence band edge in hard x-ray photoemission spectra using GW theory, J. Appl. Phys. **119**, 165703 (2016).

[26] K. van Benthem, C. Elsässer, and R. H. French, Bulk electronic structure of $SrTiO_3$: Experiment and theory, J. Appl. Phys. **90**, 6156 (2001).

[27] A. Spinelli, M. A. Torija, C. Liu, C. Jan, and C. Leighton, Electronic transport in doped $SrTiO_3$: Conduction mechanisms and potential applications, Phys. Rev. B **81**, 155110 (2010).

[28] M. S. J. Marshall, D. T. Newell, D. J. Payne, R. G. Egdell, and M. R. Castell, Atomic and electronic surface structures of dopants in oxides: STM and XPS of Nb- and La-doped $SrTiO_3$(001), Phys. Rev. B **83**, 035410 (2011).

[29] W. Meevasana, P. D. C. King, R. H. He, S. K. Mo, M. Hashimoto, A. Tamai, P. Songsiriritthigul, F. Baumberger, and Z. X. Shen, Creation and control of a two-dimensional electron liquid at the bare $SrTiO_3$ surface, Nat. Mater. **10**, 114 (2011).

[30] N. C. Plumb, M. Salluzzo, E. Razzoli, M. Månsson, M. Falub, J. Krempasky, C. E. Matt, J. Chang, M. Schulte, J. Braun, H. Ebert, J. Minár, B. Delley, K. J. Zhou, T. Schmitt, M. Shi, J. Mesot, L. Patthey, and M. Radovic, Mixed dimensionality of confined conducting electrons in the surface region of $SrTiO_3$, Phys. Rev. Lett. **113**, 086801 (2014).

[31] Z. Wang, S. M. Walker, A. Tamai, Y. Wang, Z. Ristic, F. Y. Bruno, A. de la Torre, S. Ricco, N. C. Plumb, M. Shi, P. Hlawenka, J. Sanchez-Barriga, A. Varykhalov, T. K. Kim, M. Hoesch, P. D. C. King, W. Meevasana, U. Diebold, J. Mesot, B. Moritz, T. P. Devereaux, M. Radovic, and F. Baumberger, Tailoring the nature and strength of electron-phonon interactions in the $SrTiO_3$(001) 2D electron liquid, Nat. Mater. **15**, 835 (2016).

[32] L. Dudy, M. Sing, P. Scheiderer, J. D. Denlinger, P. Schutz, J. Gabel, M. Buchwald, C. Schlueter, T. L. Lee, and R. Claessen, In situ control of separate electronic phases on $SrTiO_3$ surfaces by oxygen dosing, Adv. Mater. **28**, 7443 (2016).

[33] L. Hedin, New method for calculating the one-particle green's function with application to the electron-gas problem, Phys. Rev. **139**, A796 (1965).

[34] M. van Schilfgaarde, T. Kotani, and S. Faleev, Quasiparticle self-consistent GW theory, Phys. Rev. Lett. **96**, 226402 (2006).

[35] T. Kotani, M. van Schilfgaarde, and S. V. Faleev, Quasiparticle self-consistent GW Method: A basis for the independent-particle approximation, Phys. Rev. B **76**, 165106 (2007).

[36] D. Pashov, S. Acharya, W. R. L. Lambrecht, J. Jackson, K. D. Belashchenko, A. Chantis, F. Jamet, and M. van Schilfgaarde, Questaal: A package of electronic structure methods based on the linear muffin-tin orbital technique, Comput. Phys. Commun. **249**, 107065 (2020).

[37] B. Cunningham, M. Gruning, D. Pashov, and M. van Schilfgaarde, QSG$\widehat{W}$: Quasiparticle self-consistent *GW* with ladder diagrams in *W*, Phys. Rev. B **108**, 165104 (2023).

[38] J. P. Perdew, A. Ruzsinszky, G. I. Csonka, O. A. Vydrov, G. E. Scuseria, L. A. Constantin, X. L. Zhou, and K. Burke, Restoring the density-gradient expansion for exchange in solids and surfaces, Phys. Rev. Lett. **100**, 136406 (2008).

[39] G. Kresse and J. Furthmüller, Efficient iterative schemes for *ab initio* total-energy calculations using a plane-wave basis set, Phys. Rev. B **54**, 11169 (1996).

[40] G. Kresse and D. Joubert, From ultrasoft pseudopotentials to the projector augmented-wave method, Phys. Rev. B **59**, 1758 (1999).

[41] S. L. Dudarev, G. A. Botton, S. Y. Savrasov, C. J. Humphreys, and A. P. Sutton, Electron-energy-loss spectra and the structural stability of nickel oxide: An LSDA+U study, Phys. Rev. B **57**, 1505 (1998).

[42] S. A. Chambers, Y. Du, Z. Zhu, J. Wang, M. J. Wahila, L. F. J. Piper, A. Prakash, J. Yue, B. Jalan, S. R. Spurgeon, D. M. Kepaptsoglou, Q. M. Ramasse, and P. V. Sushko, Interconversion of intrinsic defects in $SrTiO_3$(001), Phys. Rev. B **97**, 245204 (2018).

[43] P. E. Blöchl, Projector augmented-wave method, Phys. Rev. B **50**, 17953 (1994).

[44] J. J. Yeh and I. Lindau, Atomic subshell photoionization cross sections and asymmetry parameters: $1 \leqslant Z \leqslant 103$, At. Data Nucl. Data Tables **32**, 1 (1985).

[45] M. B. Trzhaskovskaya, V. I. Nefedov, and V. G. Yarzhemsky, Photoelectron angular distribution parameters for elements $Z = 1$ to $Z = 54$ in the photoelectron energy range 100–5000 eV, At. Data Nucl. Data Tables **77**, 97 (2001).

[46] P. D. C. King, T. D. Veal, A. Schleife, J. Zúñiga-Pérez, B. Martel, P. H. Jefferson, F. Fuchs, V. Muñoz-Sanjosé, F. Bechstedt, and C. F. McConville, Valence-band electronic structure of CdO, ZnO, and MgO from x-ray photoemission spectroscopy and quasi-particle-corrected density-functional theory calculations, Phys. Rev. B **79**, 205205 (2009).

[47] S. M. Sze, *Physics of Semiconductor Devices* (John Wiley and Sons, Hoboken, NJ, 2007).

[48] R. A. McKee, F. J. Walker, M. B. Nardelli, W. A. Shelton, and G. M. Stocks, The interface phase and the Schottky barrier for a crystalline dielectric on silicon, Science **300**, 1726 (2003).

[49] S. A. Chambers, T. Ohsawa, C. M. Wang, I. Lyubinetsky, and J. E. Jaffe, Band offsets at the epitaxial anatase TiO_2-$SrTiO_3$ interface, Surf. Sci. **603**, 771 (2009).

[50] S. A. Chambers and P. V. Sushko, Influence of crystalline order and defects on the absolute work functions and electron affinities of TiO_2- and SrO-terminated *n*-$SrTiO_3$(001), Phys. Rev. Mater. **3**, 125803 (2019).

[51] G. Drera, F. Banfi, F. F. Canova, P. Borghetti, L. Sangaletti, F. Bondino, E. Magnano, J. Huijben, M. Huijben, G. Rijnders, D. H. A. Blank, H. Hilgenkamp, and A. Brinkman, Spectroscopic evidence of in-gap states at the $LaAlO_3$-$SrTiO_3$ ultrathin interfaces, Appl. Phys. Lett. **98**, 052907 (2011).

[52] A. Koitzsch, J. Ocker, M. Knupfer, M. C. Dekker, K. Dorr, B. Buchner, and P. Hoffmann, In-gap electronic structure of $LaAlO_3$-$SrTiO_3$ heterointerfaces investigated by soft x-ray spectroscopy, Phys. Rev. B **84**, 245121 (2011).

[53] G. Berner, M. Sing, H. Fujiwara, A. Yasui, Y. Saitoh, A. Yamasaki, Y. Nishitani, A. Sekiyama, N. Pavlenko, T. Kopp, C. Richter, J. Mannhart, S. Suga, and R. Claessen, Direct *k*-space mapping of the electronic structure in an oxide-oxide interface, Phys. Rev. Lett. **110**, 247601 (2013).

[54] C. Cancellieri, M. L. Reinle-Schmitt, M. Kobayashi, V. N. Strocov, T. Schmitt, P. R. Willmott, S. Gariglio, and J. M. Triscone, Interface Fermi states of $LaAlO_3$-$SrTiO_3$ and related heterostructures, Phys. Rev. Lett. **110**, 137601 (2013).

[55] P. Schutz, D. V. Christensen, V. Borisov, F. Pfaff, P. Scheiderer, L. Dudy, M. Zapf, J. Gabel, Y. Z. Chen, N. Pryds, V. A. Rogalev, V. N. Strocov, C. Schlueter, T. L. Lee, H. O. Jeschke, R. Valenti, M. Sing, and R. Claessen, Microscopic origin of the mobility enhancement at a spinel/perovskite oxide heterointerface revealed by photoemission spectroscopy, Phys. Rev. B **96**, 161409(R) (2017).

[56] J. Gabel, M. Zapf, P. Scheiderer, P. Schutz, L. Dudy, M. Stubinger, C. Schlueter, T. L. Lee, M. Sing, and R. Claessen, Disentangling specific versus generic doping mechanisms in oxide heterointerfaces, Phys. Rev. B **95**, 195109 (2017).

[57] S. A. Chambers, Z. H. Lim, J. H. Ngai, D. Biswas, and T.-L. Lee, Probing the electronic properties of gap states near the surface of N-$SrTiO_{3-\delta}$/i-Si(001) heterojunctions with high sensitivity, Phys. Rev. Mater. **8**, 014602 (2024).